IOP Publishing Phys. Med. Biol. 64 (2019) 165018 (18pp) https://doi.org/10.1088/1361-6560/ab3525

Physics in Medicine & Biology

IPEM Institute of Physics and Engineering in Medicine

RECEIVED
19 December 2018

REVISED
16 May 2019

ACCEPTED FOR PUBLICATION
24 July 2019

PUBLISHED
21 August 2019

PAPER

Fully automated gridding reconstruction for non-Cartesian x-space magnetic particle imaging

A A Ozaslan[1,2], A Alacaoglu[1,3], O B Demirel[1,2,4,5], T Çukur[1,2,6] and E U Saritas[1,2,6]

[1] Department of Electrical and Electronics Engineering, Bilkent University, Ankara, Turkey
[2] National Magnetic Resonance Research Center (UMRAM), Bilkent University, Ankara, Turkey
[3] Laboratory for Information and Inference Systems (LIONS), École Polytechnique Fédérale de Lausanne (EPFL), Lausanne, Switzerland
[4] Department of Electrical and Computer Engineering, University of Minnesota, Minneapolis, MN, United States of America
[5] Center for Magnetic Resonance Research, University of Minnesota, Minneapolis, MN, United States of America
[6] Neuroscience Program, Sabuncu Brain Research Center, Bilkent University, Ankara, Turkey

E-mail: ozaslan@ee.bilkent.edu.tr

Keywords: magnetic particle imaging, image reconstruction, gridding reconstruction, non-Cartesian trajectories

Abstract

Magnetic particle imaging (MPI) is a fast emerging biomedical imaging modality that exploits the nonlinear response of superparamagnetic iron oxide (SPIO) nanoparticles to image their spatial distribution. Previously, various scanning trajectories were analyzed for the system function reconstruction (SFR) approach, providing important insight regarding their image quality performances. While Cartesian trajectories remain the most popular choice for x-space-based reconstruction, recent work suggests that non-Cartesian trajectories such as the Lissajous trajectory may prove beneficial for improving image quality. In this work, we propose a generalized reconstruction scheme for x-space MPI that can be used in conjunction with any scanning trajectory. The proposed technique automatically tunes the reconstruction parameters from the scanning trajectory, and does not induce any additional blurring. To demonstrate the proposed technique, we utilize five different trajectories with varying density levels. Comparison to alternative reconstruction methods show significant improvement in image quality achieved by the proposed technique. Among the tested trajectories, the Lissajous and bidirectional Cartesian trajectories prove more favorable for x-space MPI, and the resolution of the images from these two trajectories can further be improved via deblurring. The proposed fully automated gridding reconstruction can be utilized with these trajectories to improve the image quality in x-space MPI.

1. Introduction

Magnetic particle imaging (MPI) is a rapidly developing imaging modality that images the spatial distribution of superparamagnetic iron oxide (SPIO) nanoparticles (Gleich and Weizenecker 2005, Weizenecker *et al* 2007, Goodwill *et al* 2012b, Saritas *et al* 2013, Bauer *et al* 2015). Based on its resolution, sensitivity, and contrast capabilities, MPI promises a wide range of imaging applications such as angiography (Weizenecker *et al* 2009, Haegele *et al* 2012, Salamon *et al* 2016, Rahmer *et al* 2017, Vaalma *et al* 2017, Bakenecker *et al* 2018), multi-color imaging (Hensley *et al* 2015, Stehning *et al* 2016, Utkur *et al* 2017, Muslu *et al* 2018, Möddel *et al* 2018, Zhong *et al* 2018), stem cell tracking (Zheng *et al* 2016, Them *et al* 2016), and functional imaging (Mason *et al* 2017).

There are two main methods for reconstructing an MPI image: system function reconstruction (SFR) and x-space reconstruction. SFR requires a lengthy calibration measurement that records the response from a point-source SPIO sample at all pre-determined pixel locations in the field-of-view (FOV) for a given MPI system and imaging parameters (Rahmer *et al* 2009, Knopp *et al* 2010a, 2010b, Rahmer *et al* 2012). The reconstruction procedure implicitly removes the system and nanoparticle non-idealities to achieve a high-resolution image of the SPIO distribution. X-space reconstruction, on the other hand, models MPI as a linear and shift-invariant (LSI) system that yields an MPI image blurred by a point spread function (PSF) (Goodwill and Conolly 2010, 2011, Lu *et al* 2013a). The image is reconstructed by assigning the speed-compensated signal to the instantaneous position

of the field free point (FFP). While a calibration scan can completely be omitted with this approach, the blurring effects of the PSF can optionally be deconvolved using a PSF obtained via imaging a point-source SPIO sample. With the LSI assumption, measuring the PSF is a significantly shorter calibration process when compared to the calibration measurement needed for SFR.

For both reconstruction methods, various trajectories can be utilized for scanning the FOV. By far the most popular trajectory used with SFR-based MPI is the Lissajous trajectory (Weizenecker *et al* 2007, Gleich *et al* 2008, Knopp *et al* 2008, Weizenecker *et al* 2009, Knopp *et al* 2010a, Buzug *et al* 2012), whereas linear trajectories that raster the FOV approximately line-by-line are most commonly utilized in conjunction with x-space reconstruction (Goodwill *et al* 2012a). Previously, the performance of different trajectories were evaluated for SFR-based MPI, and compared with the Lissajous trajectory in terms of density, speed, and image quality using a simulation framework (Knopp *et al* 2008). In addition, a simulation study proposed utilizing a radial Lissajous trajectory with SFR, demonstrating improved image quality over the conventional Lissajous trajectory for scanning with overlapping patches (Szwargulski *et al* 2015). A recent study experimentally compared the Lissajous trajectory and the bidirectional Cartesian trajectory, demonstrating similar results in terms of image quality and sensitivity (Werner *et al* 2017). For x-space reconstruction, on the other hand, one study suggested that the Lissajous trajectory might improve the overall image resolution within a similar scan time as the linear trajectories (Konkle *et al* 2013). For linear trajectories, it was recently shown that image quality can be improved by scanning the FOV in two orthogonal directions, which helps eliminate the anisotropic blur caused by the PSF (Werner *et al* 2017, Lu *et al* 2018). In theory, the same principle should be applicable to other trajectories that feature orthogonal scanning directions, such as the Lissajous trajectory. However, previous studies did not address reconstruction from non-Cartesian trajectory to a Cartesian grid for x-space MPI. Furthermore, an in-depth analysis of trajectories for x-space MPI is currently lacking.

In this work, we present a generalized reconstruction approach for both Cartesian and non-Cartesian trajectories for x-space MPI. The proposed technique is inspired by the gridding algorithms in magnetic resonance imaging (MRI), but includes fundamental modifications to adapt to the reconstruction problems in MPI. Importantly, the proposed technique automatically tunes the two critical reconstruction parameters, kernel width and image size, from the given scanning trajectory. In addition, it does not induce any additional blurring on the MPI image. Here, we demonstrate the proposed technique with simulation results for various non-Cartesian trajectories, including comparison with alternative reconstruction techniques. In addition to proposing a practical reconstruction model, we analyze the performance of the technique on five different non-Cartesian trajectories to infer about their suitability for x-space MPI. We also analyze the effects of trajectory density and sampling density on image resolution, and compare the performances of additional deblurring techniques to improve the resolution of the gridded x-space MPI images. The proposed method is a trajectory-independent and parameter-free reconstruction scheme, and the results of this work provide insight on the suitability of the non-Cartesian trajectories for x-space MPI.

2. Theory

In 3D x-space MPI theory, the images are produced on an internal reference frame formed by two vectors that are collinear and transverse to the field free point (FFP) velocity vector (Goodwill and Conolly 2011), as shown in figure 1(a). Then, the instantaneous MPI image can be decomposed into a convolution of the nanoparticle distribution with collinear and transverse PSFs, which are rotated with respect to the FFP velocity vector.

Among the two components of the PSF shown in figure 1(a), the collinear component is narrower and better behaved. Hence, this component has the capability to provide a higher resolution and higher quality MPI image (Goodwill and Conolly 2011), as shown in figure 1(c). One method to capture only the collinear component is to align the axis of the receive coil with the FFP velocity vector. This method is straightforward when the drive field is in one direction only, e.g. a drive field in the z-direction together with a single-channel receive coil sensitive along that direction. For multi-dimensional drive fields, a more practical approach is to use multiple receive coils and combine their signals to form a virtual receive coil aligned with the instantaneous FFP velocity vector (Bente *et al* 2015). In the following subsections, we briefly describe the process of extracting only the collinear image component, followed by a detailed explanation of the proposed gridding algorithm. The derivations assume ideal magnetic fields and measurements, and instantaneous alignment of the nanoparticle magnetization with the applied field. The proposed technique builds on the mathematical basis and fundamental steps of the original x-space reconstruction (i.e. speed compensation and assigning the data to instantaneous FFP position) (Goodwill and Conolly 2010, 2011), while extending it to more complicated multi-dimensional trajectories.

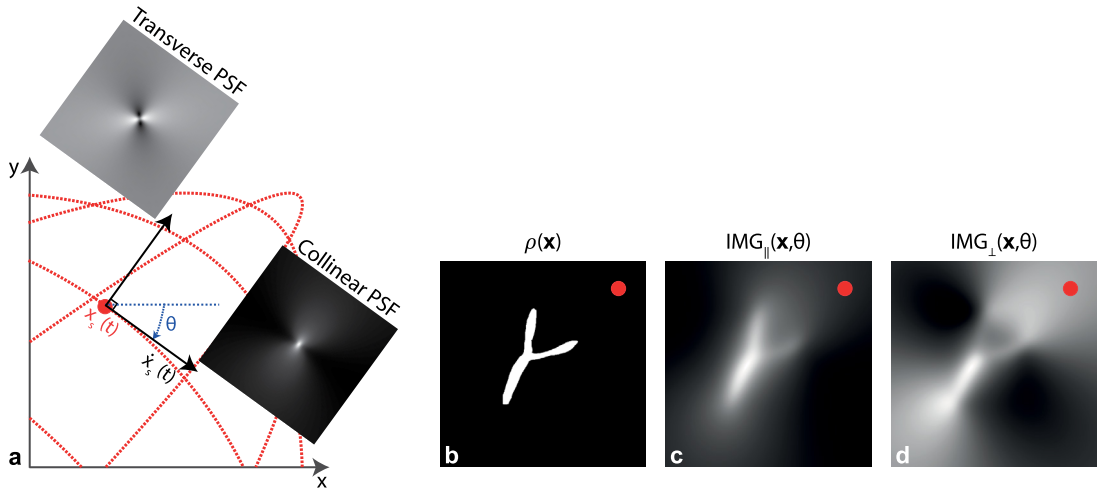

Figure 1. The collinear and transverse image components for x-space MPI. (a) The collinear and transverse PSFs for x-space MPI, rotated at an angle θ to align with the instantaneous velocity vector. Here, the FFP is following a Lissajous trajectory in x–y plane (displayed in zoomed format). (b) The nanoparticle distribution in space. (c) The collinear image and (d) the transverse image, i.e. the convolutions of the nanoparticle distribution with the collinear and transverse PSFs at angle θ, respectively. The red dot denotes the instantaneous position of the FFP.

2.1. Extraction of collinear image component

Assuming a 2D FFP trajectory in x–y plane (e.g. 2D Lissajous) together with two receive coils aligned in the physical x- and y-directions, the signals induced on the receive coils can be expressed as (Goodwill and Conolly 2011):

$$s_x(t) = B_{1,x} m \frac{\|\dot{\boldsymbol{x}}_s(t)\|}{H_{sat}} \{IMG_{\parallel}(\boldsymbol{x}_s(t), \theta(t)) \cos(\theta(t)) - IMG_{\perp}(\boldsymbol{x}_s(t), \theta(t)) \sin(\theta(t))\} \tag{1a}$$

$$s_y(t) = B_{1,y} m \frac{\|\dot{\boldsymbol{x}}_s(t)\|}{H_{sat}} \{IMG_{\parallel}(\boldsymbol{x}_s(t), \theta(t)) \sin(\theta(t)) + IMG_{\perp}(\boldsymbol{x}_s(t), \theta(t)) \cos(\theta(t))\} \tag{1b}$$

where,

$$IMG_{\parallel}(\boldsymbol{x}_s(t), \theta(t)) = \rho(\boldsymbol{x}) * h_{\parallel}(\boldsymbol{x}, \theta(t))|_{\boldsymbol{x}=\boldsymbol{x}_s(t)} \tag{2a}$$

$$IMG_{\perp}(\boldsymbol{x}_s(t), \theta(t)) = \rho(\boldsymbol{x}) * h_{\perp}(\boldsymbol{x}, \theta(t))|_{\boldsymbol{x}=\boldsymbol{x}_s(t)}\,. \tag{2b}$$

Here, $B_{1,x}$ and $B_{1,y}$ are the sensitivities of the two receive coils, m is the magnetic moment of the nanoparticle, H_{sat} is the field required for saturation, $\rho(\boldsymbol{x})$ is the nanoparticle distribution in space, $\boldsymbol{x}_s(t)$ is the FFP position vector, $\dot{\boldsymbol{x}}_s(t)$ is the FFP velocity vector, and $\theta(t)$ is the angle of the FFP velocity vector with respect to the x-axis. In addition, $h_{\parallel}(\boldsymbol{x}, \theta(t))$ and $h_{\perp}(\boldsymbol{x}, \theta(t))$ are the collinear and transverse PSFs, rotated by angle θ to align with the direction of the FFP velocity vector at time t, as demonstrated in figure 1(a). Next, $IMG_{\parallel}(\boldsymbol{x}_s(t), \theta(t))$ and $IMG_{\perp}(\boldsymbol{x}_s(t), \theta(t))$ are the collinear and transverse images as a function of FFP position at time t, as shown in figures 1(c) and (d). These images correspond to the nanoparticle distribution convolved with the collinear and transverse PSFs at time t, respectively. As seen in this figure, the collinear image displays significantly better image quality and resolution than the transverse image. Furthermore, the collinear image has better resolution along the direction of the FFP velocity vector when compared to the orthogonal direction.

Our first goal is to extract only the collinear image component from the signals $s_x(t)$ and $s_y(t)$. For this purpose, the signal for a virtual receive coil aligned with the FFP velocity vector can be computed as (Bente *et al* 2015):

$$s_v(t) = \frac{s_x(t)}{B_{1,x}} \cos(\theta(t)) + \frac{s_y(t)}{B_{1,y}} \sin(\theta(t)) \tag{3a}$$

$$= m \frac{\|\dot{\boldsymbol{x}}_s(t)\|}{H_{sat}} IMG_{\parallel}(\boldsymbol{x}_s(t), \theta(t))\,. \tag{3b}$$

In x-space MPI reconstruction, a fundamental step in image reconstruction is to compensate the received signal by the FFP speed (Goodwill and Conolly 2010, 2011). For the virtual coil, the resulting image as a function of time can then be expressed as:

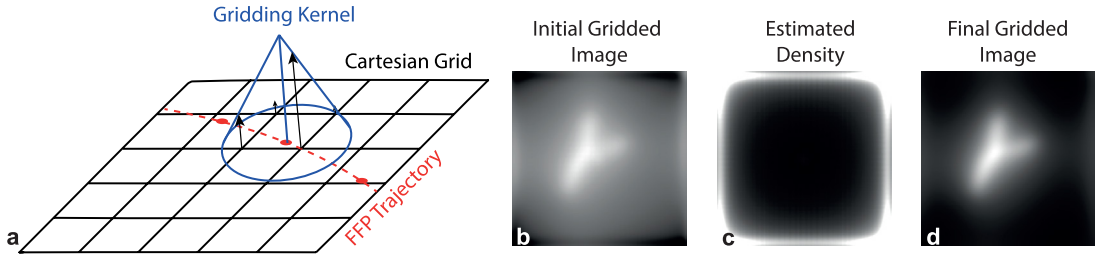

Figure 2. The proposed gridding algorithm. (a) Each data point on the FFP trajectory is convolved with the gridding kernel and re-sampled onto a Cartesian grid. (b) The initial gridded image is over-amplified at locations where the trajectory is dense. (c) The estimated density of the FFP trajectory. (d) The final gridded image is obtained via dividing the initial gridded image by the estimated density. A Lissajous trajectory was used in this example.

$$IMG_v\left(\boldsymbol{x}_s(t)\right) = \frac{s_v(t)}{\|\dot{\boldsymbol{x}}_s(t)\|} = \alpha IMG_{\|}\left(\boldsymbol{x}_s(t), \theta(t)\right). \tag{4}$$

Here, $\alpha = m/H_{sat}$ is a constant. As seen in this expression, the image from the virtual coil captures only the desired collinear component of the MPI image. In the proposed reconstruction described below, we grid only this component to achieve a higher quality x-space MPI image.

2.2. Gridding for x-space MPI

In the literature, gridding algorithms were originally proposed for the reconstruction of MRI images that utilize non-Cartesian k-space trajectories, such as radial or spiral trajectories (O'Sullivan 1985, Schomberg and Timmer 1995). These non-Cartesian trajectories provide several advantages such as motion robustness (Glover and Pauly 1992, Liao *et al* 1997), and fast data acquisition and efficient coverage of k-space (Macovski 1985, Norton 1987). In MRI gridding reconstruction, data points lying on a non-Cartesian k-space trajectory are first convolved with a kernel, and the outcome of the convolution operation is sampled and accumulated onto a Cartesian k-space grid. After density compensation of the scanning trajectory, an MRI image is produced using inverse Fourier transform, followed by apodization correction in image domain (Jackson *et al* 1991, Beatty *et al* 2005).

As opposed to MRI gridding algorithms that operate in k-space, the reconstruction in x-space MPI is performed directly in image domain. Here, we propose the following gridding algorithm for x-space image reconstruction in MPI:

$$\hat{IMG}(\boldsymbol{x}) = \frac{\hat{IMG}_{init}(\boldsymbol{x})}{\hat{d}_s(\boldsymbol{x})} = \frac{\left((IMG(\boldsymbol{x})s(\boldsymbol{x})) * c(\boldsymbol{x})\right) \cdot \text{III}\left(\frac{\boldsymbol{x}}{\Delta x}\right)}{\left(s(\boldsymbol{x}) * c(\boldsymbol{x})\right) \cdot \text{III}\left(\frac{\boldsymbol{x}}{\Delta x}\right)} \tag{5}$$

where,

$$s(\boldsymbol{x}) = \sum_{i=1}^{N_s} \delta\left(\boldsymbol{x} - \boldsymbol{x}_i\right) \tag{6a}$$

$$IMG(\boldsymbol{x_i}) = IMG_v\left(\boldsymbol{x}_s(t_i)\right), \text{ for } i = 1, \ldots, N_s. \tag{6b}$$

Here, $s(\boldsymbol{x})$ is a non-Cartesian sampling function composed of impulses placed at sampled FFP locations, $\boldsymbol{x_i} = \boldsymbol{x}_s(t_i)$. $IMG(\boldsymbol{x})$ denotes the entire image that we wish to reconstruct with values only known at sampled FFP locations, where they are equal to $IMG_v\left(\boldsymbol{x}_s(t)\right)$. In addition, $c(\boldsymbol{x})$ is the gridding kernel in x-space, $\text{III}\left(\frac{\boldsymbol{x}}{\Delta x}\right)$ is a 2D Comb function used for re-sampling onto the Cartesian grid, Δx is the spatial distance between neighboring Cartesian grid points (i.e. the resolution of the grid, assumed to be the same for x- and y-directions), and N_s is the total number of acquired samples.

As visualized in figure 2(a), the steps of the proposed gridding algorithm can be explained as follows. First, the MPI signal is obtained by scanning the FOV with an FFP trajectory, followed by the virtual coil alignment step, as described in (1)–(3). The collinear component of the MPI image, $IMG_v\left(\boldsymbol{x}_s(t)\right)$, is then captured as a function of FFP position as given in (4), which forms the sampled data, $IMG(\boldsymbol{x})s(\boldsymbol{x})$. Then, each data point on the non-Cartesian trajectory is convolved with the gridding kernel, $c(\boldsymbol{x})$, and re-sampled onto the Cartesian grid using the 2D Comb function, $\text{III}\left(\frac{\boldsymbol{x}}{\Delta x}\right)$. This initial gridded image, $\hat{IMG}_{init}(\boldsymbol{x})$, is over-amplified at locations where the trajectory is dense (see figure 2(b)). As shown in figure 2(c), an estimate of the trajectory density, $\hat{d}_s$, can be computed by gridding ones (i.e. using $IMG(\boldsymbol{x}) = 1$). Dividing the initial gridded image by the density provides the density compensated image, $\hat{IMG}(\boldsymbol{x})$, which is the final reconstructed x-space MPI image (see figure 2(d)).

For the gridding kernel, we use a Kaiser–Bessel window, which is a popular choice in MRI gridding algorithms (Beatty *et al* 2005). This kernel can be expressed as:

$$c(\boldsymbol{x}) = I_0\left(\beta\sqrt{1-\left(\frac{2\,\|\boldsymbol{x}\|}{w_k\Delta x}\right)^2}\right) \tag{7}$$

where,

$$\Delta x = \frac{x_{FOV}}{N}. \tag{8}$$

Here, $I_0(\cdot)$ is the zero-order modified Bessel function of the first kind, x_{FOV} is the extent of the FOV (assumed to be identical in x- and y-directions to simplify the notations), N is the reconstructed image size (i.e. corresponding to an $N \times N$ image for the case of 2D imaging), w_k is the full kernel width in grid units, and β denotes the shape parameter of the Kaiser–Bessel kernel. In MRI, β is chosen as a function of w_k to carefully place the zero crossings of the inverse 2DFT of the gridding kernel at the edge of the stopband. In MPI, since $c(\boldsymbol{x})$ operates directly in image domain, we do not have this concern. The choice of β for the proposed algorithm is explained in the following subsection.

2.3. Automated tuning of gridding parameters

There are fundamental differences between MRI gridding algorithms and the proposed x-space MPI gridding algorithm. First, while MRI gridding algorithms can leave certain k-space locations unfilled, the gridding in x-space MPI must spread the acquired data to all pixels on the Cartesian image grid. Secondly, the resolution of an MRI image is directly dictated by the extent of the acquired k-space, which in turn determines the image size. In contrast, there is no strict information that determines the image size or grid resolution in x-space MPI. Therefore, the kernel width (w_k) and image size (N) parameters require careful tuning to achieve high-quality x-space MPI images via the proposed technique. Here, these important parameters are computed automatically from the FFP trajectory, without manual intervention.

For computing the image size, we utilize a plane-partitioning method called Voronoi diagram. Voronoi diagrams have been utilized extensively for determining the sampling density of scanning trajectories in MRI and computed tomography (CT) (Rasche *et al* 1999). In MPI also, Voronoi diagrams were utilized to determine the areas associated with the node points of the Lissajous trajectory, to be used as weights in SFR for reconstructing an image at these nodes (Kaethner *et al* 2016). In the proposed method, we utilize Voronoi diagram for a different purpose: for determining an optimal image size directly from the trajectory data points.

Figure 3 illustrates the computation of N and w_k for the case of a Lissajous trajectory. In figure 3(b), the Voronoi diagram divides the FOV into sub-regions by bisecting the connections between each data point and its closest neighbors, which are determined using Delaunay triangulation (Rasche *et al* 1999). Following bisection, each data point is associated with a sub-region, called the Voronoi partition. For each data point on the scanning trajectory, we compute the area associated with its partition. To prevent infinitely large partitions for data points near the periphery of the trajectory, the trajectory is first surrounded by external dummy data points. Depending on the bounded shape of the scanning trajectory, these dummy data points traverse a rectangle or a circle that surrounds the trajectory. After the computation of the areas for all Voronoi partitions, the dummy points are excluded from consideration.

Using the Voronoi partitions, first we determine the image size as follows:

$$N = \left[\frac{1}{N_s}\sum_{i=1}^{N_s}\frac{x_{FOV}}{d_{V,i}}\right] = \left[\frac{1}{N_s}\sum_{i=1}^{N_s}\frac{x_{FOV}}{\sqrt{A_{V,i}}}\right]. \tag{9}$$

Here, $[\cdot]$ denotes the rounding operation and $A_{V,i}$ is the area of the Voronoi partition corresponding to the ith data point. Here, we propose that the Voronoi partition for each data point dictates the effective pixel size around that point. Approximating each Voronoi partition as a square region, $d_{V,i} = \sqrt{A_{V,i}}$ yields the effective edge size for the ith Voronoi partition. We consider this edge size to be the local pixel size associated with the ith data point. Next, a corresponding image size is computed via dividing FOV by this edge size. Finally, the mean over all data points is computed to reach the final image size, N. The corresponding pixel size for the Cartesian grid, Δx, can then be computed using (8). Following the aforementioned steps, $N \times N$ Cartesian grid points can be positioned in space, as shown in figure 3.

Next, we tune the kernel width, w_k. To do this, we reason that the kernel should be sufficiently wide to ensure that no grid points are left unfilled after gridding, but not overly wide to induce unnecessary image blurring. First, for each grid point in the image, the distance to the nearest data point is calculated as follows:

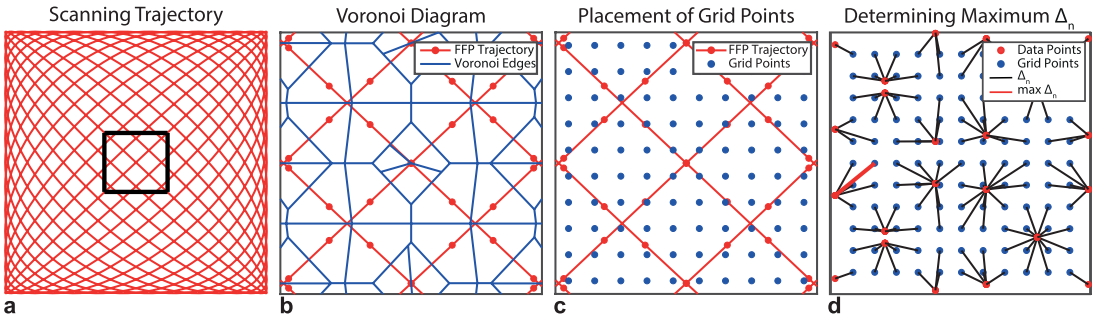

Figure 3. The proposed steps for tuning the kernel width and grid size directly from the FFP trajectory. (a) An example Lissajous trajectory with a frequency ratio of 17/16. The subsequent subfigures zoom in on the region marked with the black box. (b) A Voronoi diagram is used to calculate the areas associated with each data point on the FFP trajectory. The grid size, N, is computed using the effective edge sizes from all partitions. (c) $N \times N$ Cartesian grid points are placed on the FOV. (d) For each grid point, the distance to the nearest data point, Δ_n, is computed. The optimal kernel width is chosen as a multiple of the maximum Δ_n.

$$\Delta_n = \min_{i \in 1:N_s} \frac{\|\boldsymbol{x_n} - \boldsymbol{x_i}\|}{\Delta x}. \tag{10}$$

Here, $\boldsymbol{x_i}$ is the location of the ith data point, $\boldsymbol{x_n}$ is the location of the nth grid point, and Δ_n is the distance in grid units between the nth grid point and the nearest data point. This operation is performed for each grid point, as shown in figure 3(d). Next, the kernel width is chosen as a multiple of the maximum Δ_n, i.e.

$$w_k = \gamma \cdot \max_{n \in \Omega^2} \Delta_n. \tag{11}$$

Here, Ω^2 denotes the image grid and γ is a constant to ensure that w_k is sufficiently large to spread not just one but multiple data points to each grid point. Our analysis on γ revealed that values between 5–6 yield artifact-free images while preserving the resolution of the gridded images. Hence, in the rest of this work, we utilize $\gamma = 6$ (see the appendix for a detailed explanation of this choice).

Finally, we choose the shape parameter, β, for the Kaiser–Bessel window given in (7). This parameter is chosen to ensure that: (1) the full kernel width, w_k, tightly covers the full shape of the Kaiser–Bessel window, and (2) the full width at half maximum (FWHM) of the kernel, $FWHM_k$, is equal to half the kernel width, i.e.:

$$FWHM_k \approx \frac{w_k}{2} \Delta x. \tag{12}$$

Both of these criteria are satisfied for $\beta = 6$, which provides an efficient representation of the gridding kernel as shown in figure 4.

2.4. Deblurring of reconstructed images

The resulting images from the gridding algorithm are blurred by the collinear and transverse PSFs. Here, to improve the resolution of the reconstructed images, an optional post-processing step can be performed following the gridding reconstruction. Two candidate methods for deblurring the images are the equalization filter (Lu *et al* 2015, Lu 2015) and Wiener deconvolution.

The equalization filter is a k-space filter inspired by the ramp filter in computed tomography (CT), which is used to eliminate the background haze due to overemphasis of the low-frequency data resulting from projections. In x-space MPI, a similar overemphasis of low spatial frequencies occurs due to the wide 'normal envelope' component of the PSFs. The equalization filter was originally proposed for multichannel acquisitions where two separate images are acquired using a single-channel drive field that is 90° rotated during the second acquisition. These two images are then averaged, resulting in an isotropic blur with the following effective PSF:

$$h_{iso}(\boldsymbol{x}) = h_{\|}(\boldsymbol{x}, 0^\circ) + h_{\|}(\boldsymbol{x}, 90^\circ). \tag{13}$$

It was previously shown that this PSF can also be expressed as $E_T(\boldsymbol{x}) + 2E_N(\boldsymbol{x})$ (Lu *et al* 2013b, 2018), where $E_T(\boldsymbol{x})$ and $E_N(\boldsymbol{x})$ are the tangential and the normal envelopes of the PSFs as defined in Goodwill and Conolly (2011). The equalization filter aims to eliminate image haze by decomposing the effective PSF into its tangential and normal components, and extracting the narrower tangential component only. This filter is applied to the reconstructed MPI images in k-space (i.e. multiplied with the Fourier transform of the image, followed by inverse Fourier transformation). For multichannel acquisition, this filter is formulated as (Lu 2015):

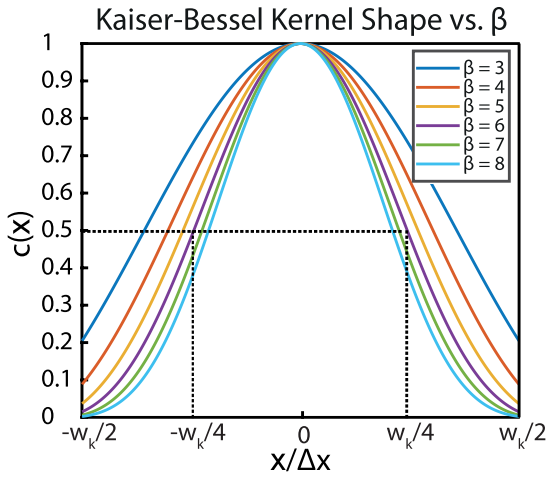

Figure 4. The shape of the Kaiser–Bessel window depends on the shape parameter β. When $\beta = 6$ (purple line), the Kaiser–Bessel window tightly covers the full kernel width and its FWHM is approximately equal to $w_k/2$ in grid units.

$$\Phi_{eq}(\boldsymbol{k}) = \frac{\mathcal{F}\left(E_T(\boldsymbol{x})\right)}{\mathcal{F}\left(E_T(\boldsymbol{x}) + 2E_N(\boldsymbol{x})\right)} \tag{14}$$

where $\mathcal{F}$ is the Fourier transform operator. It should be noted that equalization does not aim to fully deconvolve the effects of the imaging PSF. Instead, as seen in (14), the goal is to improve the effective PSF from $E_T(\boldsymbol{x}) + 2E_N(\boldsymbol{x})$ to $E_T(\boldsymbol{x})$. In contrast to standard deconvolution filters, this filter does not cause division by zero problems at high spatial frequencies where the SNR is typically low.

The equalization filter can potentially be suitable for the Lissajous and bidirectional Cartesian trajectories, as they are composed of two approximately orthogonal scanning directions. For these trajectories, the overall PSF of the imaging system can be heuristically approximated as $h_{iso}(\boldsymbol{x})$ (Goodwill 2010). Following a similar idea, this PSF can also be utilized for Wiener deconvolution. The corresponding Wiener deconvolution filter in k-space can then be formulated as follows:

$$G_w(\boldsymbol{k}) = \frac{H_{iso}{}^*(\boldsymbol{k})}{|\, H_{iso}(\boldsymbol{k})\,|^2 + NSR}. \tag{15}$$

Here, $H_{iso}(\boldsymbol{k})$ is the Fourier transform of $h_{iso}(\boldsymbol{x})$, * denotes the conjugation operation, and NSR is the noise-power-to-signal-power ratio, added to the denominator to avoid excessive noise amplification.

3. Materials and methods

3.1. Trajectories

In this work, the proposed gridding algorithm is applied to five non-Cartesian trajectories, as illustrated in figure 5: Lissajous, bidirectional Cartesian, radial Lissajous, spiral, and radial trajectories. The mathematical expressions for the trajectories are given in table 1. The choice of trajectories was guided by an earlier trajectory analysis work on SFR-based MPI (Knopp *et al* 2008, Szwargulski *et al* 2015), with the addition of the radial Lissajous trajectory. Considering hardware feasibility of the bidirectional Cartesian trajectory, a modification was performed over the theoretical version presented in table 1: the abrupt switch that occurs at multiples of half-period time points were smoothed to reach a more realistic trajectory in terms of hardware constraints, as shown in figure 5. To the best of our knowledge, among the tested trajectories, only the Lissajous trajectory has been utilized in existing MPI hardware. The bidirectional Cartesian trajectory was only utilized as two orthogonal linear acquisitions (Werner *et al* 2017, Lu *et al* 2018), and not as shown in figure 5.

The important parameters in table 1 are the fundamental drive field frequency, f_0, and the trajectory density parameter, N_P. The parameter N_P determines the frequency ratio between the two orthogonal drive channels. For all five trajectories listed, larger N_P values result in a denser FFP trajectory.

3.2. Simulations

The simulations were performed on a custom MPI toolbox developed in MATLAB (Mathworks, Natick, MA). The performance of the proposed gridding algorithm was tested on three separate imaging phantoms: a vasculature phantom, a resolution phantom, and a Derenzo phantom. An FFP scanner with selection field gradients of

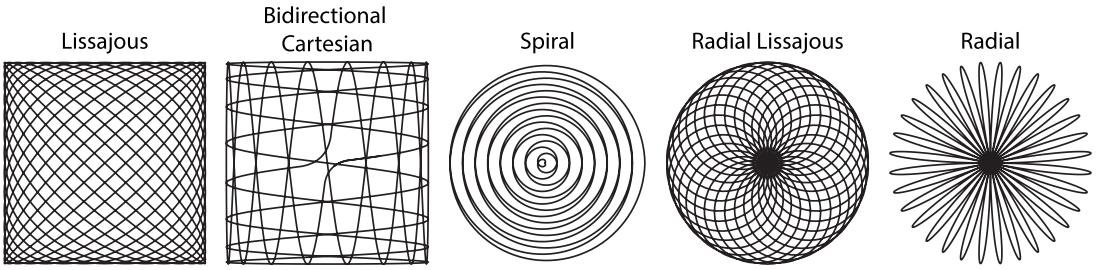

Figure 5. The non-Cartesian FFP Trajectories used in this work, all shown here for $N_P = 16$ and identical T_R.

Table 1. The mathematical expressions for the non-Cartesian FFP trajectories used in this work. The 2D drive fields and frequency ratios to generate the corresponding trajectories are given. f_0 is the fundamental drive field frequency, N_P is the trajectory density parameter, and $T_R = N_P/f_0$ is one period of the trajectory. A and B correspond to the drive field amplitudes in x- and y-directions, respectively.

Trajectories	Mathematical expression	Frequency ratio
Lissajous	$H_x(t) = A\sin(2\pi f_0 t)$ $H_y(t) = B\sin(2\pi f_1 t + \phi)$	$f_0 = \frac{N_P}{N_P-1} f_1$
Bidirectional Cartesian	$H_x(t) = \begin{cases} A\sin(2\pi f_0 t), & t < \frac{T_R}{2} \\ B\sin(2\pi f_1 t + \phi), & t \geqslant \frac{T_R}{2} \end{cases}$ $H_y(t) = \begin{cases} A\sin(2\pi f_1 t + \phi), & t < \frac{T_R}{2} \\ B\sin(2\pi f_0 t), & t \geqslant \frac{T_R}{2} \end{cases}$	$f_0 = \frac{N_P}{2} f_1$
Spiral	$H_x(t) = A\sin(2\pi f_1 t)\cdot\cos(2\pi f_0 t)$ $H_y(t) = B\sin(2\pi f_1 t)\cdot\sin(2\pi f_0 t)$	$f_0 = N_P f_1$
Radial Lissajous	$H_x(t) = A\sin(2\pi f_0 t)\cdot\sin(2\pi f_1 t)$ $H_y(t) = B\sin(2\pi f_1 t)\cdot\cos(2\pi f_0 t)$	$f_0 = \frac{N_P}{N_P-1} f_1$
Radial	$H_x(t) = A\sin(2\pi f_0 t)\cdot\sin(2\pi f_1 t)$ $H_y(t) = B\sin(2\pi f_1 t)\cdot\cos(2\pi f_0 t)$	$f_0 = N_P f_1$

$(3, 3, -6)\,T/m/\mu_0$ in the (x, y, z) directions and a drive field amplitude of 30 mT in both x- and y-directions were assumed, corresponding to a FOV of 2×2 cm^2 in the x–y plane. A realistic nanoparticle diameter of 25 nm was assumed (Ferguson *et al* 2015, Kaul *et al* 2017). The MPI signal for a single cycle of each trajectory was generated for a fundamental drive field frequency of $f_0 = 25$ kHz with 2.5 MS s^{-1} sampling rate. For the Lissajous and bidirectional Cartesian trajectories, $\phi = 0$ was used (see table 1). Before the reconstruction, the signal was filtered using a high pass filter with a cut-off frequency of $1.8 \times f_0$ to completely remove the fundamental harmonic.

3.3. Alternative reconstructions

The proposed technique was compared with two different x-space-based reconstruction methods to interpolate the given non-Cartesian data onto the Cartesian grid: scattered interpolation and scattered interpolation with trajectory partitioning (Alacaoglu *et al* 2016). In general, scattered interpolation first triangulates the given data using Delaunay triangulation. The vertices of the triangle enclosing each query point (i.e. the grid points) are lifted to obtain the weights corresponding to the data points. Using natural-neighbor interpolation, lifted triangles are then interpolated to obtain the optimal image intensity for the grid point enclosed by the triangle (Amidror 2002).

Using the aforementioned scattered interpolation, two alternative reconstruction techniques were implemented:

(i) **Scattered interpolation**: The data points and the FFP trajectory are directly fed to the interpolation algorithm.

(ii) **Scattered interpolation with partitioning**: The trajectory is partitioned into two non-overlapping segments with nearly orthogonal directions. Next, an image for each partition is reconstructed using scattered interpolation, and the resulting images are averaged to obtain the final MPI image (Alacaoglu *et al* 2016). The two segments are at approximately 45° and 135° scanning angles for the Lissajous trajectory, and 0° and 90° scanning angles for the bidirectional Cartesian trajectory. Note that this method cannot be applied to the other tested trajectories, as they cannot be partitioned into a few different angles.

These comparison techniques used a fixed grid size of 512 × 512, independent of the trajectory type and density level.

3.4. Image quality analysis

The proposed technique was further analyzed for the Lissajous and the bidirectional Cartesian trajectories at twenty different trajectory density levels between 10 and 200. Note that the density of the data points for an already acquired data can also be artificially altered by upsampling/downsampling the time-domain signal. To test the potential effects of such alterations, the sampled signal for a Lissajous trajectory was spline interpolated/decimated using 9 different sampling factors ranging between 0.25 and 4. This step was performed after the filtering of the fundamental harmonic.

To quantify the effects on image resolution, the FWHM resolution metric was utilized. As dictated by imaging theory (Prince and Links 2006), the effective FWHM resolution of the reconstructed MPI image, $FWHM_m$, can be approximated as:

$$FWHM_m = \sqrt{FWHM_s^2 + FWHM_k^2}. \tag{16}$$

Here, $FWHM_s$ is the native resolution of the MPI system, mainly governed by the selection field gradients and nanoparticle properties, and $FWHM_k$ is the FWHM of the gridding kernel as given in (12). The above equation suggests that the effective resolution of the MPI image worsens with increasing kernel width, and the level of resolution loss depends on the relative magnitude of the kernel width with respect to the native resolution. As explained in section 2.4, the PSF for the Lissajous and bidirectional Cartesian trajectories can be approximated as the isotropic PSF, $h_{iso}(\boldsymbol{x})$. As there is no closed form expression for the FWHM of $h_{iso}(\boldsymbol{x})$, it can be computed numerically from a central cross-section of $h_{iso}(\boldsymbol{x})$. Accordingly, for the parameters used in this work, $FWHM_s$ is approximately equal to 2.06 mm.

Next, to quantify the effects of trajectory density and sampling factor on overall image quality, the peak signal-to-noise ratio (PSNR) metric was utilized:

$$PSNR = 10\, log_{10}\left(\frac{\max^2(\rho)}{MSE}\right). \tag{17}$$

Here, $\rho(\boldsymbol{x})$ is the numeric phantom (i.e. the nanoparticle distribution) used in the simulations and MSE is the mean square error between the phantom and the reconstructed image. Here, higher values of PSNR indicate improved image quality.

3.5. Deblurring and noise robustness

To show potential improvements in the gridded images, both the equalization filter (Lu *et al* 2015) and Wiener deconvolution methods were implemented for the Lissajous and the bidirectional Cartesian trajectories. As explained in section 2.4, the equalization filter aims to improve the effective PSF from $h_{iso}(\boldsymbol{x})$ to $E_T(\boldsymbol{x})$. For the parameters used in this work, this corresponds to an improvement of the effective FWHM from 2.06 mm to 1.47 mm, where the latter is the approximate FWHM of $E_T(\boldsymbol{x})$ as given in Goodwill and Conolly (2011). For Wiener deconvolution, $NSR = 1 \times 10^{-5}$ was utilized.

Prior to performing deblurring via equalization or deconvolution, the reconstructed MPI image was first extended in all four directions by replicating the edges, and the resulting image was gradually faded to zero in the extended regions (Yorulmaz *et al* 2018). After deblurring, the central part of the image was extracted to capture the original FOV. These edge-tapering steps were necessary for avoiding deblurring-induced artifacts at the edges of the FOV.

Noise robustness of the proposed gridding technique and the subsequent deblurring methods were tested at four different signal-to-noise ratio (SNR) levels (50, 20, 10, and 5) using the Lissajous trajectory. White Gaussian noise was added to the simulated signal after the filtering of the fundamental harmonic. Here, SNR was defined as the ratio of the peak signal (after filtering) and the standard deviation of the additive white Gaussian noise.

4. Results

4.1. Reconstruction results and trajectory evaluation

Reconstruction results for the proposed algorithm and the comparison techniques can be seen in figures 6 and 7 for $N_P = 50$. Figure 6 shows the Lissajous and bidirectional Cartesian trajectories, together with the resulting MPI images. The isotropically blurred image, IMG_{iso}, obtained via convolving the phantom with $h_{iso}(\boldsymbol{x})$ in (14), is also displayed for visual comparison. Note that IMG_{iso} is the MPI image that would be obtained with the standard x-space reconstruction using two orthogonal linear trajectories (Lu *et al* 2018). As seen in figure 6, directly performing scattered interpolation yields images with abruptly changing pixel intensities. These severe artifacts

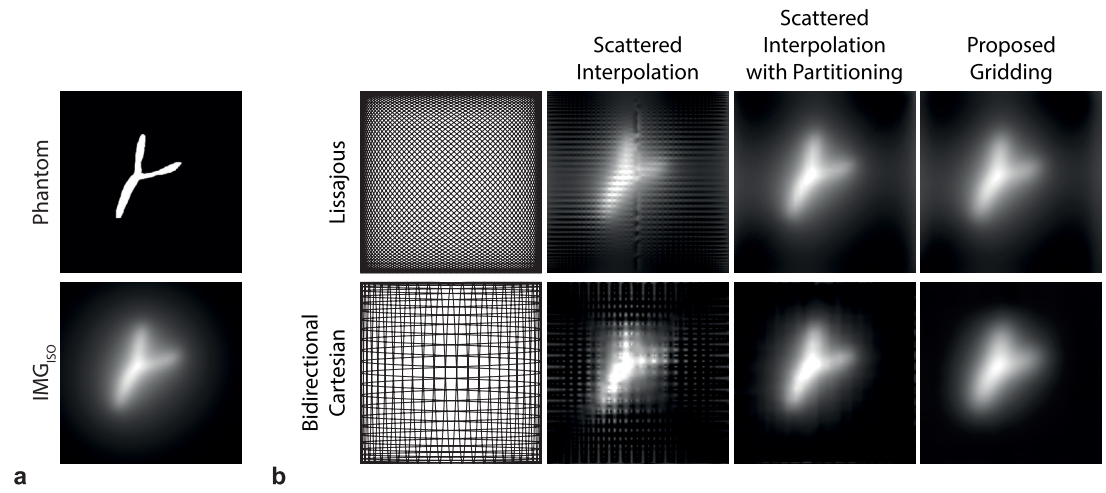

Figure 6. Reconstruction results for the Lissajous and bidirectional Cartesian trajectories. (a) The phantom and the isotropically blurred image, obtained via convolution with $h_{iso}(\boldsymbol{x})$ in (14). (b) Scattered interpolation causes severe artifacts due to the different scanning directions of nearby data points. While partitioning the data before applying scattered interpolation removes these artifacts, horizontal and vertical stripe artifacts can still be observed. The proposed method does not suffer from any of the aforementioned artifacts, and reconstructs the image by automatically tuning the reconstruction parameters from the scanning trajectory. The results closely match IMG_{iso} for both trajectories. For these simulations, the FOV was 2×2 cm^2 and $N_P = 50$. For each trajectory, the images from all three methods were displayed with identical windowing.

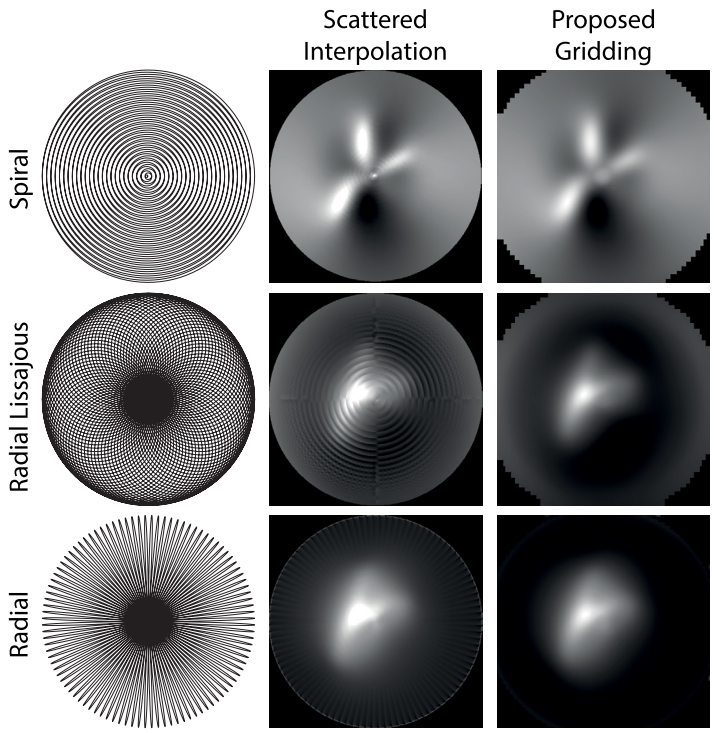

Figure 7. Reconstruction results for the trajectories that cannot be partitioned. Images from scattered interpolation have artifacts in the central regions of the images where the trajectories are very dense. Ring-shaped artifacts are observed for the spiral and radial Lissajous trajectories, and streak artifacts are seen for the radial trajectory. The proposed gridding algorithm successfully removes all of these artifacts. However, trajectory-induced smearing results in noticeably blurred MPI images. For these simulations, the FOV was 2×2 cm^2 and $N_P = 50$. For each trajectory, the images from both methods were displayed with identical windowing.

stem from the fact that the nearby data points on a trajectory can be inconsistent when their scanning directions are different, as the x-space images corresponding to those data points are blurred by distinct PSFs. When data are first partitioned into two non-overlapping segments, the severe artifacts seen in direct scattered interpolation are avoided. However, a closer inspection of these images reveals horizontal and vertical stripe artifacts, which are caused by inconsistencies between the images reconstructed from the two separate partitions. The proposed gridding algorithm, on the other hand, does not suffer from any of the aforementioned artifacts and reconstructs the x-space MPI image by automatically determining the reconstruction parameters from the MPI data. The

resulting images closely match IMG_{iso} for both trajectories. As a trade-off, when compared to the results of scattered interpolation with partitioning, the proposed method induced a slight blurring on the reconstructed images. While this blurring is caused by the interpolation kernel used in gridding, it can be circumvented by appropriate choice of trajectory density and/or sampling factor, as shown in later analyses.

Figure 7 shows the reconstructed MPI images for the trajectories that cannot be partitioned, i.e. the spiral, radial Lissajous, and radial trajectories. These trajectories scan the FOV in varying directions, and unlike the Lissajous or bidirectional Cartesian trajectories, they do not feature any main scanning directions. Therefore, the only comparison technique considered here was the direct scattered interpolation method. For the scattered interpolation, the image artifacts occur mostly in the central regions of the images where the trajectories are very dense. Ring-shaped artifacts can be observed for the spiral and radial Lissajous trajectories, whereas the radial trajectory suffers from streak artifacts extending radially from the center of the image. Again, these artifacts stem from inconsistencies among nearby data points. The proposed gridding algorithm successfully removes all of these artifacts. However, the resulting images display noticeable blurring when compared to the results from the Lissajous or bidirectional Cartesian trajectories for the same N_P. Note that the exact same blurring is also present in scattered interpolation results, indicating that it is not caused by the gridding interpolation. It rather reflects a trajectory-induced smearing of the MPI image.

Considering their superior performance, only the Lissajous and bidirectional Cartesian trajectories were considered for subsequent analyses.

4.2. Effects of trajectory density

To observe the effects of the trajectory density, N_P, on the quality of the reconstructed images, the signal acquisition process was simulated for four different N_P values: 18, 30, 50, and 98. The resulting images are shown in figure 8(a). For the Lissajous trajectory, the vasculature structure can be distinguished even at low density values. For the bidirectional Cartesian trajectory, however, the resolution at very low densities is visibly degraded. Note that the bidirectional Cartesian trajectory is inherently much sparser than the Lissajous trajectory, because the effective trajectory density is reduced by a factor of two to keep the repetition times identical among all trajectories (see the 1/2 factor in table 1 for the frequency ratio of the bidirectional Cartesian trajectory) (Knopp *et al* 2008). For both trajectories, as the density of the trajectory is increased, the resolution of the gridded MPI image improves. This effect is quantified in figures 8(b) and (c), where the automatically computed values for the image size (N) and the effective gridding kernel width (i.e. $FWHM_k$ in (12)) are plotted as functions of N_P, for both the Lissajous and the bidirectional Cartesian trajectories. As expected, N increases with increasing N_P, as the local pixel size dictated by the Voronoi partitions of the data points gets smaller. Furthermore, with increasing N_P, the minimum distance between each grid point and the nearest data point is reduced. This in turn lowers $FWHM_k$ to ensure adequate spread of data points onto nearby grids.

The values for $FWHM_m$ computed using (16) are also plotted in figure 8(c). For both trajectories, $FWHM_m$ converges to 2.27 mm for increasing N_P values. Hence, we deduce that when $FWHM_k$ is sufficiently smaller than $FWHM_s$, the gridding algorithm does not induce any significant blur on the reconstructed images. This criterion is satisfied for $N_P > 50$ for the Lissajous trajectory and for $N_P > 90$ for the bidirectional Cartesian trajectory.

Image quality was also quantified using the PSNR metric, as shown in figure 8(d). For both trajectories, image quality sharply increases until N_P reaches 40. Then, PSNR gradually converges to 12.9 dB for the Lissajous trajectory. For the bidirectional Cartesian trajectory, PSNR displays a slowly increasing trend and reaches to 13.4 dB at $N_P = 200$. The bidirectional Cartesian trajectory performs slightly better than the Lissajous trajectory because of its blurring pattern that yields lower image haze in the background. Note that the PSNR value for IMG_{iso} in figure 6(a) is 12.4 dB. Hence, the quality of the images from the proposed gridded algorithm can exceed those obtained with linear trajectories via standard x-space reconstruction.

4.3. Effects of sampling factor

In MPI, the density of the data points not only depend on the path of the trajectory, but also on the sampling rate of the signal. Even for a fixed sampling rate, one can artificially alter the density of the data points by upsampling/downsampling the signal. Figure 9(a) shows the FWHM of the gridding kernel as a function of both the trajectory density and the sampling factor, for an initial sampling rate of 2.5 MS s^{-1}. Accordingly, for a fixed trajectory density, one can reduce the effective kernel width by upsampling the MPI signal. Figure 9(b) shows the effects of this procedure on the overall resolution of the gridded MPI image. For N_P values greater than approximately 40, upsampling can be utilized to achieve an overall resolution of 2.11 mm, which closely matches the native resolution. In most cases, a sampling factor of 2 is sufficient to avoid any blurring of the MPI image. A similar trend is seen in the PSNR values shown in figure 9(c), where PSNR converges to 13.0 dB with a sampling factor of 2 and $N_P > 50$. These results are visually demonstrated in figure 9(d), where gridded MPI images at four different sampling factors are displayed for $N_P = 98$. Here, a sampling factor of 2 provides noticeable improvements in

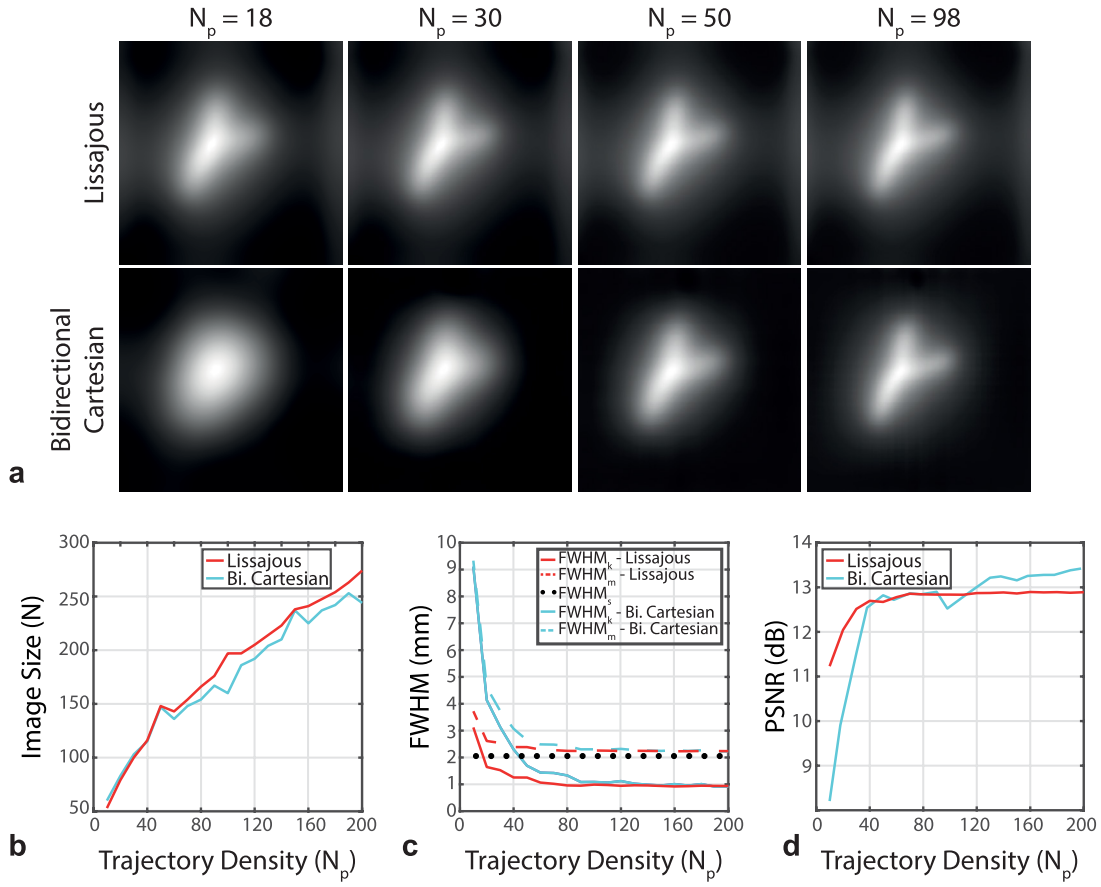

Figure 8. The effects of trajectory density, N_P, on the reconstructed MPI images. (a) The results of the gridding algorithm for the Lissajous and bidirectional Cartesian trajectories for $N_P = 18, 30, 50$, and 98. As N_P is increased, the resolution of the gridded MPI image improves for both trajectories. (b) The image size (N) that is automatically tuned using the MPI trajectory monotonically increases with increasing N_P. (c) The FWHM of the gridding kernel decreases and then converges to a constant value as N_P increases. The overall image resolution ($FWHM_m$) also improves and converges to the native resolution of the MPI system ($FWHM_s$) with increasing N_P. (d) The overall image quality improves and rapidly converges to a constant PSNR value for both trajectories as N_P increases.

image resolution, and suffices to avoid gridding-induced blurring. A sampling factor of 4 does not provide any additional benefits on the image quality.

4.4. Deblurring and noise robustness

The resolution of the x-space reconstructed images can be improved via a post-processing step, following gridding. Figure 10 illustrates the resolution improvement achieved by applying either an equalization filter or Wiener deconvolution on the gridded images. A 2×2 cm^2 phantom, shown in figure 10(a), was utilized to highlight the changes in resolution. Both the Lissajous and bidirectional Cartesian trajectories utilized $N_P = 98$. The signal was generated with an initial sampling rate of 2.5 MS s^{-1} and upsampled with a sampling factor of 2. As seen in figure 10(b), the equalization filter significantly improves the resolution of the image. Using (14), for the parameters used in this work, this filter aims to improve the effective FWHM from 2.06 mm to 1.47 mm. The deconvolved images in figure 10(b) show greater improvement in resolution, at the expense of potential noise amplification, as analyzed in detail below. In comparing trajectories, both the equalization and deconvolution techniques gave slightly improved results for the Lissajous trajectories, which is to be expected given the lower effective density of the bidirectional Cartesian trajectory.

Figure 11 gives the results for the noise robustness analyses for both the gridding reconstruction and the deblurring techniques. Again, the Lissajous trajectory with $N_P = 98$ was used, and data acquisition was performed at 2.5 MS s^{-1} with a sampling factor of 2. For these analyses, we utilized the Derenzo phantom shown in figure 11(a) with five resolution levels: 3.9 mm, 3.2 mm, 2.5 mm, 2.0 mm, and 1.4 mm. In the noise free case in figure 11(b), the disks that are at 2.5 mm or higher separation are visually resolved in the gridded image. After the equalization filter, the resolution improves visibly and the disks at 2.0 mm separation can also be resolved visually. While Wiener deconvolution further improves the resolution, the disks at 1.4 mm remain unresolved. As seen in figure 11(b), the gridding reconstruction shows robustness against noise down to SNR levels of 10. At high SNR levels, Wiener deconvolution yields improved image quality and higher resolution when compared

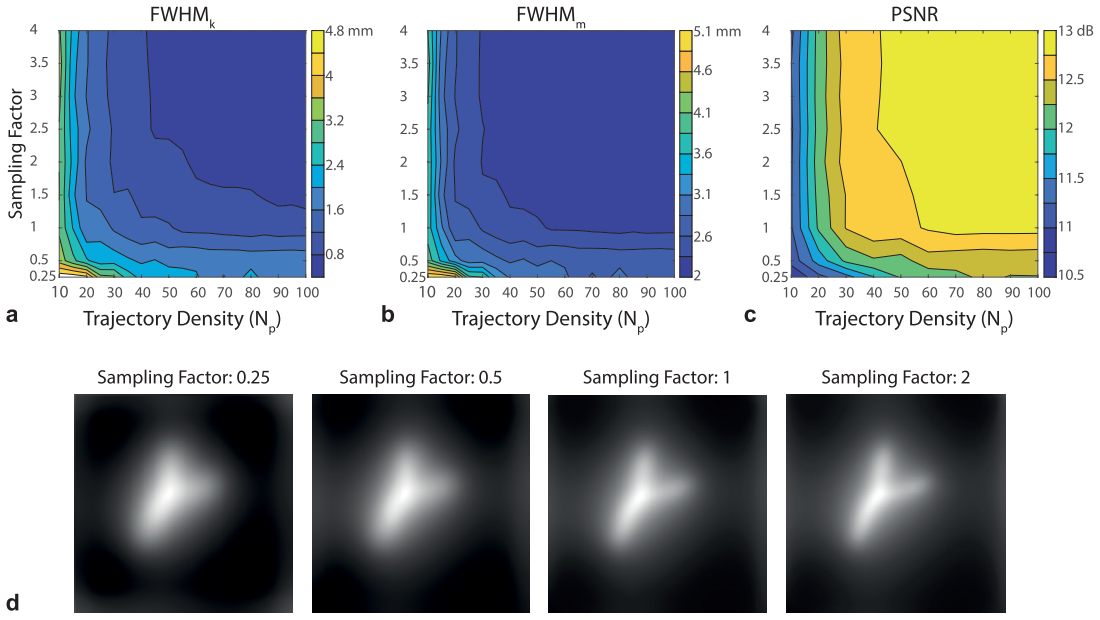

Figure 9. Effects of upsampling/downsampling the MPI signal. (a) The FWHM of the gridding kernel quickly decreases and (b) the overall image resolution converges to the native system resolution for increasing trajectory density and sampling factor. (c) The overall image quality also improves with increasing trajectory density and sampling factor, where PSNR converges to 13.0 dB. (d) The gridded MPI images at $N_P = 98$ for different sampling factors. A sampling factor of 2 suffices to avoid gridding-induced blurring. For these simulations, the initial sampling rate was 2.5 MS s^{-1} and the Lissajous trajectory was utilized.

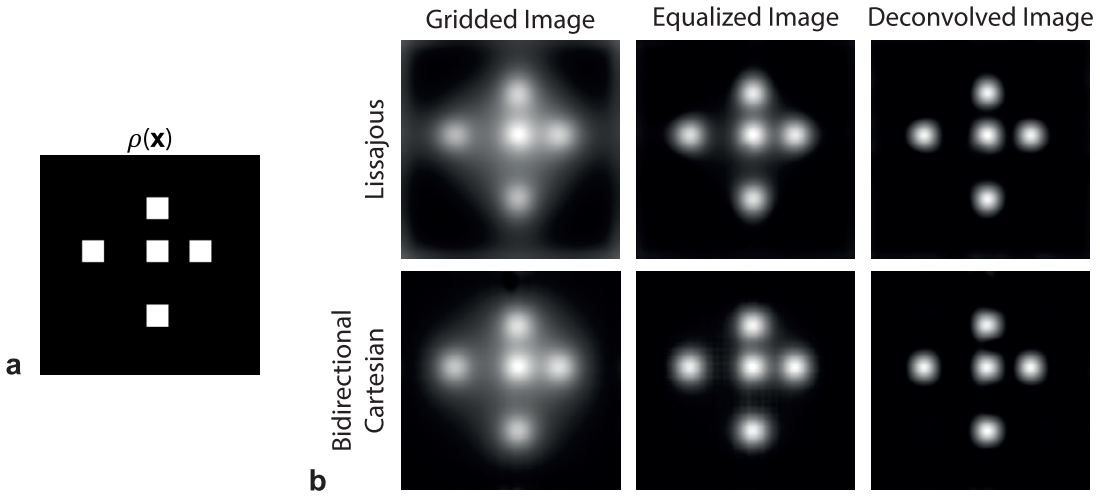

Figure 10. Postprocessing results for the proposed gridding algorithm. (a) The phantom and (b) the results of the gridding algorithm followed by either an equalization filter or Wiener deconvolution. The gridded images can be significantly improved in terms of resolution using either of these two postprocessing techniques. Equalization does not aim to fully deconvolve the effects of the imaging PSF. For these simulations, FOV $= 2 \times 2$ cm^2 and $N_P = 98$, with 2.5 MS s^{-1} sampling rate and a sampling factor of 2.

to the equalization filter. At SNR levels around 20 and lower, however, the equalization filter displays improved robustness against artifacts and noise amplification when compared to Wiener deconvolution. The noise amplification in the deconvolved image is clearly visible at SNR $= 5$, where the background noise competes with image intensity. Note that these results are displayed for a single cycle of the Lissajous trajectory, with a scan time of merely 3.92 ms. Significant improvements in image quality can easily be achieved by increasing the SNR via averaging over multiple cycles.

5. Discussion

The proposed gridding algorithm successfully reconstructs MPI images for non-Cartesian trajectories, while automatically computing the reconstruction parameters from the FFP trajectory. Among the tested trajectories, the Lissajous and bidirectional Cartesian trajectories resulted in higher image quality, whereas spiral, radial, and

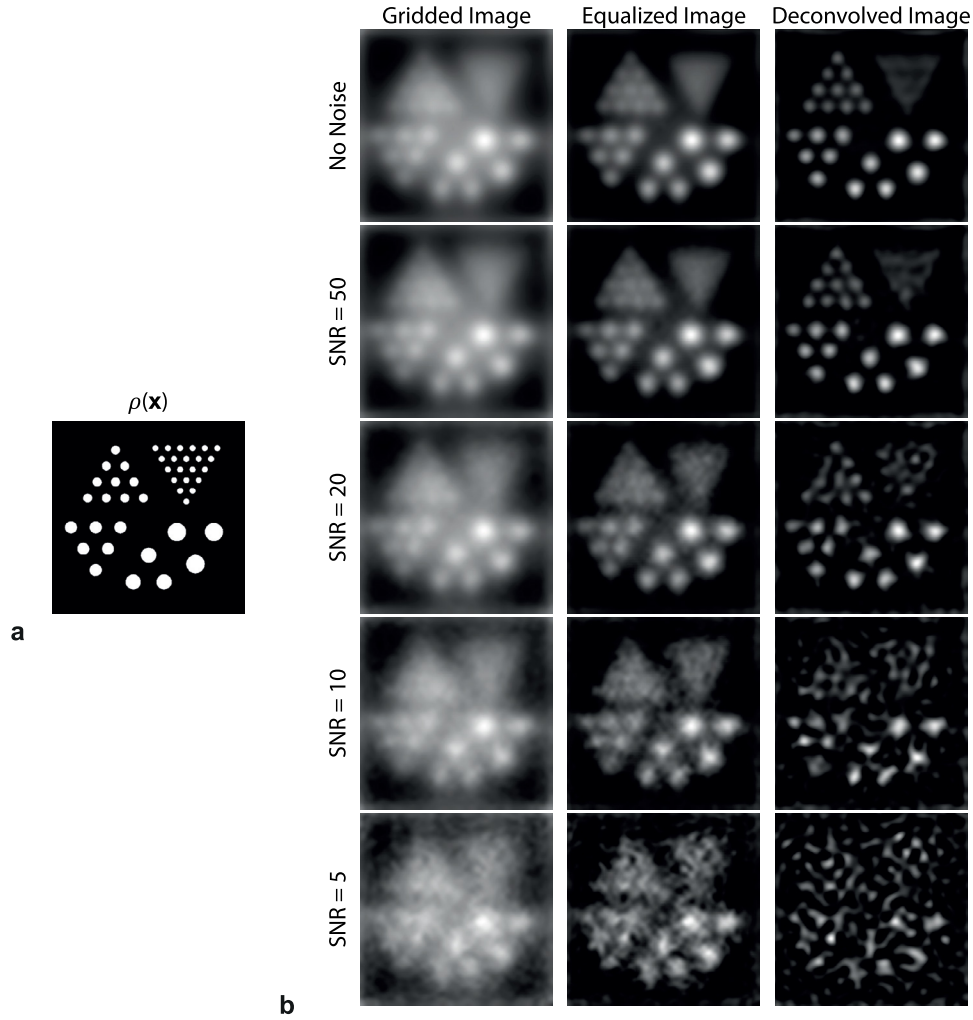

Figure 11. Noise robustness results for the proposed gridding algorithm and the postprocessing techniques. (a) A Derenzo phantom with five resolution levels: 3.9 mm, 3.2 mm, 2.5 mm, 2.0 mm, and 1.4 mm. (b) The gridding algorithm preserves image quality down to SNR levels of 10. Wiener deconvolution yields higher image resolution at high SNR levels, whereas the equalization filter displays improved robustness against artifacts and noise amplification at lower SNR levels. For these simulations, FOV $= 2 \times 2$ cm^2 and $N_P = 98$, with 2.5 MS s^{-1} sampling rate and a sampling factor of 2.

radial Lissajous trajectories yielded excessive blurring. The advantage of the Lissajous and bidirectional Cartesian trajectories is that they are composed of two nearly orthogonal scanning directions. In contrast, spiral, radial, and radial Lissajous trajectories incorporate scanning directions that result in smearing of the MPI image. Note that this result is consistent with earlier work that looked at trajectory analysis for SFR, where the Lissajous and Cartesian trajectories resulted in improved resolution when compared to other trajectories (Knopp *et al* 2008). Hence, we deduce that the Lissajous and Cartesian trajectories are generally favorable for MPI.

The results demonstrate that the gridded images can be improved via a simple upsampling of the already acquired MPI signal. This simple operation increases the effective trajectory density and helps the proposed method to achieve the native resolution of the MPI system. It should also be noted that directly sampling the signal at 5 MS s^{-1} yields visually identical results to sampling at 2.5 MS s^{-1} followed by upsampling by a factor of 2 (results not shown). Therefore, considering the fact that the MPI signal quickly fades at higher harmonics, the signal can be sampled at a relatively low rate followed by upsampling, without compromising image quality. In addition, deblurring techniques also help improve the resolution of the reconstructed images. The equalization filter removes the background haze, without noise amplification. Deconvolution, on the other hand, improves the resolution at the expense of significant degradation in SNR. Therefore, especially at realistic SNR levels one may expect to see for *in vivo* imaging, the equalization filter shows a better promise.

The proposed method provides a reconstruction with reduced memory and computational requirements for the trajectories normally utilized with SFR. In SFR, the system matrix contains the calibration data and is of size $(N_f \times N_c \times 2) \times (N \times N)$, where $(N \times N)$ denotes the imaging FOV matrix, N_f is the number of frequency components, N_c is the number of receive coils, and real and imaginary components of the spectrum are stored in separate rows. For a typical scenario with $N = 40$, $N_f = 10\,000$, $N_c = 2$, approximately 512 MB of memory is

needed for the system matrix alone. Meanwhile, the actual imaging data in both the SFR and x-space approaches (including the proposed method) form a vector of length $(N_s \times N_c \times 2)$, where N_s is the number of samples collected in one period of the trajectory (assuming that repeated periods are first averaged). For $N_s = 10\,000$, approximately 32 MB of memory is needed for the imaging data. Thus, the memory requirement of the x-space approach is substantially smaller than that of the SFR approach (~32 MB versus ~544 MB for the given parameters). In terms of computational efficiency, previous studies suggest that algebraic reconstruction technique (ART), which is currently the most popular reconstruction method in SFR, is expected to be of complexity $O(N_f \times N_c \times N_{iter} \times N^2)$, where N_{iter} is the number of iterations (Knopp *et al* 2010a, Li *et al* 2015). While there have been several efforts to reduce the computational complexity of the SFR approach, the N^2 dependence still remains (Knopp and Hofmann 2016, Schmiester *et al* 2017, Kluth and Jin 2019). For the proposed gridding algorithm, on the other hand, the two main steps are the Voronoi partitioning and the gridding operations. Common algorithms for Voronoi partitioning are of complexity $O(N_s \log(N_s))$ (Leach 1992, Edelsbrunner and Shah 1996). In the gridding stage, the samples on the trajectory are distributed to their nearest grid points. Assuming that $N_g \ll N_s$ samples will be distributed on average to each grid point, this bears a complexity of $O(N_g \times N^2)$ (O'Sullivan 1985). Hence, the proposed gridding method is advantageous in terms of memory storage, with comparable computational efficiency.

With the abovementioned advantages, the proposed gridding technique is especially promising for real-time imaging applications that require the usage of a rapid scanning trajectory with a rapid image reconstruction method. Trajectories such as the Lissajous trajectory can achieve higher frame rates when compared to line-by-line scanning. In contrast to SFR approaches, the proposed gridding algorithm does not require any calibration scans, and hence can potentially handle arbitrary changes in FOV, trajectory density, nanoparticle type, or nanoparticle environment. These features may especially be valuable for real-time imaging applications where one may need to change the size and/or the position of the FOV on the fly (e.g. during interventional imaging), or where the nanoparticle response may change over time (e.g. due to internalization into a cell environment (Zheng *et al* 2015, Them *et al* 2016). For optional deblurring of the reconstructed image, one may need to perform a calibration scan to determine the PSF from a point source phantom. Nevertheless, this procedure takes significantly less time when compared to the calibration of the system matrix. In addition, this technique can enable x-space reconstruction of Lissajous data obtained from existing commercial MPI scanners, which may then facilitate the usage of other x-space-based techniques on those systems (e.g. relaxation-based color MPI (Muslu *et al* 2018)).

The results in this work assumed that nanoparticle magnetization instantaneously aligns with the applied magnetic field. Nanoparticle relaxation can smear the MPI signal, and hence the image, along the scanning direction. For example, the two dominant directions for the Lissajous trajectory may yield images that are smeared differently. For those cases, one solution can be to perform a low-level correction for relaxation by compensating for relaxation induced signal delays (Croft *et al* 2012). Alternatively, the effective time constant for relaxation can be estimated from the MPI signal (Utkur *et al* 2017, Muslu *et al* 2018), and the underlying adiabatic MPI signal can be recovered via deconvolution (Bente *et al* 2015). A potential problem that may remain is the position-dependent response of the nanoparticles, which may especially afflict the Lissajous trajectory with its fast field rotation. For such cases, it may be favorable to utilize isotropic nanoparticles with small hydrodynamic diameters, as suggested in Graeser *et al* (2015). Alternatively, a class of nanoparticles with reduced relaxation effects despite their larger sizes may also be utilized, such as UW33 in Croft *et al* (2016).

The non-ideality of the magnetic fields may also affect the quality of the reconstructed images. For standard x-space reconstruction, we have previously shown that selection fields with non-homogeneous gradients result in geometric warping of the reconstructed images (Yagiz *et al* 2019). These effects are relatively benign and can be successfully corrected using image unwarping techniques, following a measurement and/or computation of the displacement map. Similarly, we expect the proposed gridding algorithm to yield images with easily reversible warping in the presence of selection field non-ideality, making it extendable to 3D imaging. Experimental validation of the proposed technique and its extension to 3D remain as important future work.

6. Conclusion

In this work, we proposed a generalized, trajectory-independent, and parameter-free reconstruction algorithm for x-space MPI. The proposed gridding algorithm automatically tunes gridding kernel width and image size parameters based on the scanning trajectory, without causing any additional blurring of the MPI image. The results demonstrate that the Lissajous and bidirectional Cartesian trajectories are favorable for x-space MPI, as they feature two orthogonal scanning directions that result in an approximately isotropic PSF. The proposed method is especially promising for real-time imaging applications that require rapid scanning trajectories together with a rapid image reconstruction method.

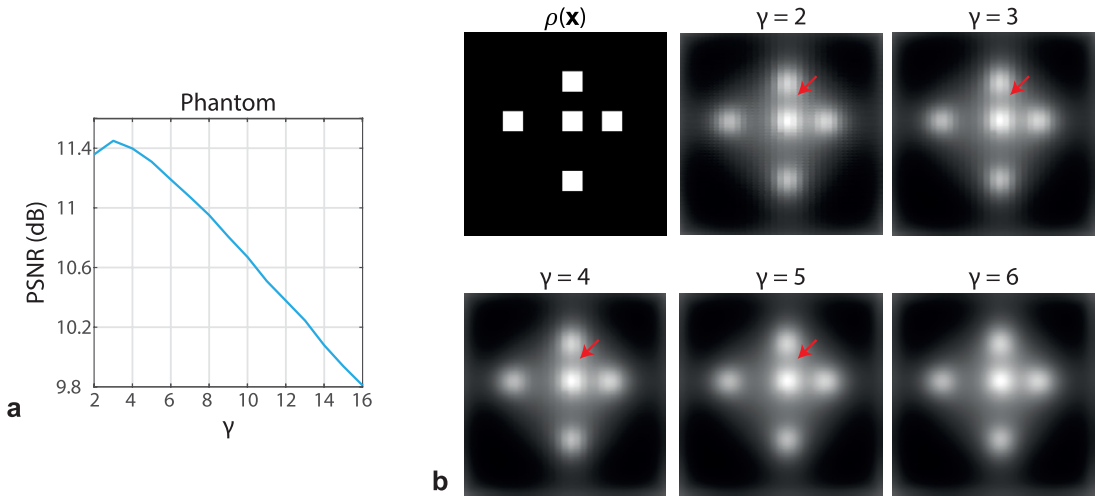

Figure A1. The effect of γ on image quality. (a) PSNR analysis indicates that highest image quality is achieved at $\gamma = 3$, with higher γ values causing a reduction in image quality. (b) The phantom and the results of the gridding algorithm for various γ values. Vertical stripe artifacts not captured by the PSNR metric are clearly visible in the reconstructed image for $\gamma = 3$ (red arrow). These artifacts diminish at higher γ values, however, the image resolution also worsens simultaneously. Here, the choice of $\gamma = 6$ corresponds to the smallest integer-valued γ that yields artifact-free images.

Acknowledgments

A preliminary version of this work was presented at the 8th International Workshop on Magnetic Particle Imaging (IWMPI 2018). This work was supported by the Turkish Academy of Sciences through TUBA-GEBIP 2015 program, and by the Science Academy through BAGEP award.

Appendix

This appendix explains the choice of γ, the multiplicative parameter in (11) that controls the kernel width. This parameter was determined based on two factors: quantitative image quality assessment via the PSNR metric and visual inspection. The results of the PSNR assessment are given in figure A1(a) for the Lissajous trajectory at $N_p = 98$ with a sampling factor of 1. The phantom used in this assessment is displayed in figure A1(b) together with the results of the gridding algorithm at various γ values. The PSNR assessment implies that higher γ values result in reduced image quality, with $\gamma = 3$ yielding the highest PSNR. However, the corresponding image visibly suffers from vertical stripe artifacts (shown by red arrows), which are remnants of the scanning trajectory. As γ increases, the intensity of this artifact weakens and finally disappears for γ greater than 5–6. On the other hand, a higher γ value directly corresponds to a higher $FWHM_k$, causing an increased blurring in the reconstructed image. The PSNR metric successfully captures this reduction in resolution for higher γ values, but fails to detect the artifacts seen at lower γ values. To prevent such artifacts while preserving the resolution of the reconstructed images, we choose $\gamma = 6$, which is the smallest integer-valued γ that yields artifact-free images.

ORCID iDs

A A Ozaslan https://orcid.org/0000-0003-4067-2904
A Alacaoglu https://orcid.org/0000-0002-2911-7048
O B Demirel https://orcid.org/0000-0003-4726-0590
T Çukur https://orcid.org/0000-0002-2296-851X
E U Saritas https://orcid.org/0000-0001-8551-1077

References

Alacaoglu A, Ozaslan A A and Saritas E U 2016 Nonlinear scanning in x-space MPI *Int. Workshop on Magnetic Particle Imaging* (*Book of Abstracts*) (Lübeck) p 74

Amidror I 2002 Scattered data interpolation methods for electronic imaging systems: a survey *J. Electron. Imaging* **11** 157–77

Bakenecker A C, Ahlborg M, Debbeler C, Kaethner C, Buzug T M and Lüdtke-Buzug K 2018 Magnetic particle imaging in vascular medicine *Innovative Surg. Sci.* **3** 179–92

Bauer L M, Situ S F, Griswold M A and Samia A C S 2015 Magnetic particle imaging tracers: state-of-the-art and future directions *J. Phys. Chem. Lett.* **6** 2509–17

Beatty P J, Nishimura D G and Pauly J M 2005 Rapid gridding reconstruction with a minimal oversampling ratio *IEEE Trans. Med. Imaging* **24** 799–808
Bente K, Weber M, Graeser M, Sattel T F, Erbe M and Buzug T M 2015 Electronic field free line rotation and relaxation deconvolution in magnetic particle imaging *IEEE Trans. Med. Imaging* **34** 644–51
Buzug T M *et al* 2012 Magnetic particle imaging: introduction to imaging and hardware realization *Z. Med. Phys.* **22** 323–34
Croft L R, Goodwill P W and Conolly S M 2012 Relaxation in x-space magnetic particle imaging *IEEE Trans. Med. Imaging* **31** 2335–42
Croft L R, Goodwill P W, Konkle J, Arami H, Price D A, Li A X, Saritas E U and Conolly S M 2016 Low drive field amplitude for improved image resolution in magnetic particle imaging *Med. Phys.* **43** 424–35
Edelsbrunner H and Shah N R 1996 Incremental topological flipping works for regular triangulations *Algorithmica* **15** 223–41
Ferguson R M *et al* 2015 Magnetic particle imaging with tailored iron oxide nanoparticle tracers *IEEE Trans. Med. Imaging* **34** 1077–84
Gleich B and Weizenecker J 2005 Tomographic imaging using the nonlinear response of magnetic particles *Nature* **435** 1214–7
Gleich B, Weizenecker J and Borgert J 2008 Experimental results on fast 2D-encoded magnetic particle imaging *Phys. Med. Biol.* **53** N81–4
Glover G H and Pauly J M 1992 Projection reconstruction techniques for reduction of motion effects in MRI *Magn. Reson. Med.* **28** 275–89
Goodwill P 2010 Narrowband and x-space magnetic particle imaging *PhD Thesis* (Berkeley, CA: UC Berkeley)
Goodwill P W and Conolly S M 2010 The x-space formulation of the magnetic particle imaging process: 1D signal, resolution, bandwidth, SNR, SAR, and magnetostimulation *IEEE Trans. Med. Imaging* **29** 1851–9
Goodwill P W and Conolly S M 2011 Multidimensional x-space magnetic particle imaging *IEEE Trans. Med. Imaging* **30** 1581–90
Goodwill P W, Lu K, Zheng B and Conolly S M 2012a An x-space magnetic particle imaging scanner *Rev. Sci. Instrum.* **83** 033708
Goodwill P W, Saritas E U, Croft L R, Kim T N, Krishnan K M, Schaffer D V and Conolly S M 2012b X-space MPI: magnetic nanoparticles for safe medical imaging *Adv. Mater.* **24** 3870–7
Graeser M, Bente K, Neumann A and Buzug T 2015 Trajectory dependent particle response for anisotropic mono domain particles in magnetic particle imaging *J. Phys. D: Appl. Phys.* **49** 045007
Haegele J, Rahmer J, Gleich B, Bontus C, Borgert J, Wojtczyk H, Buzug T M, Barkhausen J and Vogt F M 2012 Visualization of instruments for cardiovascular intervention using MPI *Magnetic Particle Imaging Springer Proc. in Physics* vol 140 (Berlin: Springer) pp 211–5
Hensley D, Goodwill P, Croft L and Conolly S 2015 Preliminary experimental x-space color MPI *5th Int. Workshop on Magnetic Particle Imaging (Istanbul, Turkey, 26–28 March 2015)* (IEEE) p 1
Jackson J I, Meyer C H, Nishimura D G and Macovski A 1991 Selection of a convolution function for Fourier inversion using gridding *IEEE Trans. Med. Imaging* **10** 473–8
Kaethner C, Erb W, Ahlborg M, Szwargulski P, Knopp T and Buzug T M 2016 Non-equispaced system matrix acquisition for magnetic particle imaging based on Lissajous node points *IEEE Trans. Med. Imaging* **35** 2476–85
Kaul M *et al* 2017 *In vitro* and *in vivo* comparison of a tailored magnetic particle imaging blood pool tracer with Resovist *Phys. Med. Biol.* **62** 3454–69
Kluth T and Jin B 2019 Enhanced reconstruction in magnetic particle imaging by whitening and randomized SVD approximation *Phys. Med. Biol.* **64** 125026
Knopp T and Hofmann M 2016 Online reconstruction of 3D magnetic particle imaging data *Phys. Med. Biol.* **61** N257
Knopp T, Biederer S, Sattel T, Weizenecker J, Gleich B, Borgert J and Buzug T 2008 Trajectory analysis for magnetic particle imaging *Phys. Med. Biol.* **54** 385
Knopp T, Rahmer J, Sattel T, Biederer S, Weizenecker J, Gleich B, Borgert J and Buzug T 2010a Weighted iterative reconstruction for magnetic particle imaging *Phys. Med. Biol.* **55** 1577
Knopp T, Sattel T F, Biederer S, Rahmer J, Weizenecker J, Gleich B, Borgert J and Buzug T M 2010b Model-based reconstruction for magnetic particle imaging *IEEE Trans. Med. Imaging* **29** 12–8
Konkle J J, Goodwill P W, Saritas E U, Zheng B, Lu K and Conolly S M 2013 Twenty-fold acceleration of 3D projection reconstruction MPI *Biomed. Tech./Biomed. Eng.* **58** 565–76
Leach G 1992 Improving worst-case optimal Delaunay triangulation algorithms *4th Canadian Conf. on Computational Geometry p* 15
Li S, Chan C, Stockmann J P, Tagare H, Adluru G, Tam L K, Galiana G, Constable R T, Kozerke S and Peters D C 2015 Algebraic reconstruction technique for parallel imaging reconstruction of undersampled radial data: application to cardiac cine *Magn. Reson. Med.* **73** 1643–53
Liao J R, Pauly J M, Brosnan T J and Pelc N J 1997 Reduction of motion artifacts in cine MRI using variable-density spiral trajectories *Magn. Reson. Med.* **37** 569–75
Lu K 2015 Linearity, shift-invariance and resolution improvement for quantitative magnetic particle imaging *PhD Thesis* (Berkeley, CA: UC Berkeley)
Lu K, Goodwill P W, Saritas E U, Zheng B and Conolly S M 2013a Linearity and shift invariance for quantitative magnetic particle imaging *IEEE Trans. Med. Imaging* **32** 1565–75
Lu K, Goodwill P, Zheng B and Conolly S 2015 Reshaping the 2D MPI PSF to be isotropic and sharp using vector acquisition and equalization *5th Int. Workshop on Magnetic Particle Imaging (Istanbul, Turkey, 26–28 March 2015)* (IEEE) p 1
Lu K, Goodwill P, Zheng B and Conolly S 2018 Multi-channel acquisition for isotropic resolution in magnetic particle imaging *IEEE Trans. Med. Imaging* **37** 1989–98
Lu K, Zheng B, Konkle J, Saritas E, Goodwill P and Conolly S 2013b Towards multidimensional x-space magnetic particle imaging for improved resolution *Int. Workshop on Magnetic Particle Imaging (Berkeley, CA: 23–24 March 2013)* (IEEE) p 1
Macovski A 1985 Volumetric NMR imaging with time-varying gradients *Magn. Reson. Med.* **2** 29–40
Mason E E, Cooley C Z, Cauley S F, Griswold M A, Conolly S M and Wald L L 2017 Design analysis of an MPI human functional brain scanner *Int. J. Magn. Part. Imaging* **3** 1703008
Möddel M, Meins C, Dieckhoff J and Knopp T 2018 Viscosity quantification using multi-contrast magnetic particle imaging *New J. Phys.* **20** 083001
Muslu Y, Utkur M, Demirel O B and Saritas E U 2018 Calibration-free relaxation-based multi-color magnetic particle imaging *IEEE Trans. Med. Imaging* **37** 1920–31
Norton S J 1987 Fast magnetic resonance imaging with simultaneously oscillating and rotating fiell gradients *IEEE Trans. Med. Imaging* **6** 21–31
O'Sullivan J D 1985 A fast sinc function gridding algorithm for Fourier inversion in computer tomography *IEEE Trans. Med. Imaging* **4** 200–7
Prince J L and Links J M 2006 *Medical Imaging Signals and Systems* (Upper Saddle River, NJ: Pearson Prentice Hall)
Rahmer J, Weizenecker J, Gleich B and Borgert J 2009 Signal encoding in magnetic particle imaging: properties of the system function *BMC Med. Imaging* **9** 4

Rahmer J, Weizenecker J, Gleich B and Borgert J 2012 Analysis of a 3D system function measured for magnetic particle imaging *IEEE Trans. Med. Imaging* **31** 1289–99
Rahmer J, Wirtz D, Bontus C, Borgert J and Gleich B 2017 Interactive magnetic catheter steering with 3D real-time feedback using multi-color magnetic particle imaging *IEEE Trans. Med. Imaging* **36** 1449–56
Rasche V, Proksa R, Sinkus R, Börnert P and Eggers H 1999 Resampling of data between arbitrary grids using convolution interpolation *IEEE Trans. Med. Imaging* **18** 385–92
Salamon J *et al* 2016 Magnetic particle / magnetic resonance imaging: *in vitro* MPI-guided real time catheter tracking and 4D angioplasty using a road map and blood pool tracer approach *PLoS One* **11** e0156899
Saritas E U, Goodwill P W, Croft L R, Konkle J J, Lu K, Zheng B and Conolly S M 2013 Magnetic particle imaging (MPI) for NMR and MRI researchers *J. Magn. Reson.* **229** 116–26
Schmiester L, Möddel M, Erb W and Knopp T 2017 Direct image reconstruction of Lissajous-type magnetic particle imaging data using Chebyshev-based matrix compression *IEEE Trans. Comput. Imaging* **3** 671–81
Schomberg H and Timmer J 1995 The gridding method for image reconstruction by Fourier transformation *IEEE Trans. Med. Imaging* **14** 596–607
Stehning C, Gleich B and Rahmer J 2016 Simultaneous magnetic particle imaging (MPI) and temperature mapping using multi-color MPI *Int. J. Magn. Part. Imaging* **2** 1612001
Szwargulski P, Kaethner C, Ahlborg M and Buzug T 2015 A radial Lissajous trajectory for magnetic particle imaging *5th Int. Workshop on Magnetic Particle Imaging (Istanbul, Turkey, 26–28 March 2015)* (IEEE) p 1
Them K, Salamon J, Szwargulski P, Sequeira S, Kaul M G, Lange C, Ittrich H and Knopp T 2016 Increasing the sensitivity for stem cell monitoring in system-function based magnetic particle imaging *Phys. Med. Biol.* **61** 3279–90
Utkur M, Muslu Y and Saritas E U 2017 Relaxation-based viscosity mapping for magnetic particle imaging *Phys. Med. Biol.* **62** 3422
Vaalma S, Rahmer J, Panagiotopoulos N, Duschka R L, Borgert J, Barkhausen J, Vogt F M and Haegele J 2017 Magnetic particle imaging (MPI): experimental quantification of vascular stenosis using stationary stenosis phantoms *PLoS One* **12** e0168902
Weizenecker J, Borgert J and Gleich B 2007 A simulation study on the resolution and sensitivity of magnetic particle imaging *Phys. Med. Biol.* **52** 6363–74
Weizenecker J, Gleich B, Rahmer J, Dahnke H and Borgert J 2009 Three-dimensional real-time *in vivo* magnetic particle imaging *Phys. Med. Biol.* **54** L1
Werner F, Gdaniec N and Knopp T 2017 First experimental comparison between the Cartesian and the Lissajous trajectory for magnetic particle imaging *Phys. Med. Biol.* **62** 3407
Yagiz E, Utkur M, Eren O C and Saritas E U 2019 Selection-field-induced warping in x-space MPI *Int. Workshop on Magnetic Particle Imaging (New York, 17–19 March 2019)* (*Book of Abstracts*) p 74
Yorulmaz O, Demirel O B, Çukur T, Saritas E U and Çetin A E 2018 A blind deconvolution technique based on projection onto convex sets for magnetic particle imaging (arXiv:1705.07506 [physics.med-ph])
Zheng B, Vazin T, Goodwill P W, Conway A, Verma A, Saritas E U, Schaffer D and Conolly S M 2015 Magnetic particle imaging tracks the long-term fate of *in vivo* neural cell implants with high image contrast *Sci. Rep.* **5** 14055
Zheng B, Von See M P, Yu E, Gunel B, Lu K, Vazin T, Schaffer D V, Goodwill P W and Conolly S M 2016 Quantitative magnetic particle imaging monitors the transplantation, biodistribution, and clearance of stem cells *in vivo Theranostics* **6** 291–301
Zhong J, Schilling M and Ludwig F 2018 Magnetic nanoparticle temperature imaging with a scanning magnetic particle spectrometer *Meas. Sci. Technol.* **29** 115903